







Article

Growth Process, Structure and Electronic Properties of Cr₂GeC and Cr_{2-x}Mn_xGeC Thin Films Prepared by Magnetron Sputtering

Anton S. Tarasov ^{1,*}, Sergey A. Lyaschenko ^{1,*}, Mikhail V. Rautskii ¹, Anna V. Lukyanenko ¹, Tatiana A. Andryushchenko ¹, Leonid A. Solovyov ², Ivan A. Yakovlev ¹, Olga A. Maximova ¹, Dmitriy V. Shevtsov ¹, Mikhail A. Bondarev ¹, Ilya A. Bondarev ^{1,3}, Sergei G. Ovchinnikov ¹, and Sergey N. Varnakov ^{1,3}

¹ Kirensky Institute of Physics, Federal Research Center KSC SB RAS, 660036 Krasnoyarsk, Russia; lav@iph.krasn.ru (A.V.L.); bia@iph.krasn.ru (I.A.B.)

² Institute of Chemistry and Chemical Technology, Federal Research Center KSC SB RAS, 660036 Krasnoyarsk, Russia

³ Krasnoyarsk Scientific Center, Federal Research Center KSC SB RAS, 660036 Krasnoyarsk, Russia

* Correspondence: taras@iph.krasn.ru (A.S.T.); isa@iph.krasn.ru (S.A.L.)

Abstract: The growth and phase formation features, along with the influence of structure and morphology on the electronic, optical, and transport properties of Cr₂GeC and Cr_{2-x}Mn_xGeC MAX phase thin films synthesized by magnetron sputtering technique, were studied. It was found that the Cr:Ge:C atomic ratios most likely play the main role in the formation of a thin film of the MAX phase. A slight excess of carbon and manganese doping significantly improved the phase composition of the films. Cr₂GeC films with a thicknesses exceeding 40 nm consisted of crystallites with well-developed facets, exhibiting metallic optical and transport properties. The hopping conduction observed in the Cr_{2-x}Mn_xGeC film could be attributed to the columnar form of crystallites. Calculations based on a two-band model indicated high carrier concentrations *N*, *P* and mobility *μ* in the best-synthesized Cr₂GeC film, suggesting transport properties close to single crystal material. The findings of this study can be utilized to enhance the growth technology of MAX phase thin films.

Keywords: MAX phase; thin film; magnetron sputtering; electronic transport; optical spectra



Citation: Tarasov, A.S.; Lyaschenko, S.A.; Rautskii, M.V.; Lukyanenko, A.V.; Andryushchenko, T.A.; Solovyov, L.A.; Yakovlev, I.A.; Maximova, O.A.; Shevtsov, D.V.; Bondarev, M.A.; et al. Growth Process, Structure and Electronic Properties of Cr₂GeC and Cr_{2-x}Mn_xGeC Thin Films Prepared by Magnetron Sputtering. *Processes* **2023**, *11*, 2236. <https://doi.org/10.3390/pr11082236>

Academic Editor: Anna Paola Caricato

Received: 26 June 2023

Revised: 16 July 2023

Accepted: 22 July 2023

Published: 25 July 2023



Copyright: © 2023 by the authors. Licensee MDPI, Basel, Switzerland. This article is an open access article distributed under the terms and conditions of the Creative Commons Attribution (CC BY) license (<https://creativecommons.org/licenses/by/4.0/>).

1. Introduction

Since the discovery of graphene [1], there has been a growing interest in two-dimensional and layered materials, including hexagonal boron nitride [2], transition metal chalcogenides [3], as well as MAX phases and their derivatives, such as MXenes [4–6]. MAX phases belong to a family of layered hexagonal compounds with the general formula M_{n+1}AX_n, where M is an early transition element (e.g., Sc, Ti, V, Mn, Cr, Zr, Nb, Mo, Hf, Ta), A is an A-group element from group 13 or 14 (e.g., Al, P, S, Ga, Ge, As, Cd, In, Sn, Tl, Pb), X is carbon or nitrogen [3]. One of the conditions for the stability of such multilayered structures is the alternation of chemical bonding types between M–X–M and M–A–M. This alternation leads to a number of interesting physical properties in the material, such as a combination of metallic and ceramic properties (electron conductivity along M–X layers, hardness, and chemical stability) and significant magnetostriction perpendicular to the M–X layers [7]. Being layered materials, MAX phases exhibit strong anisotropy in conductivity [8], thermal conductivity [9], elastic and strength properties [10]. In addition to thermal, chemical, and mechanical stability, MAX phases also demonstrate radiation resistance [11,12], making them practically versatile protective coatings. Particular interest in magnetic MAX phases is associated with the prospects of two-dimensional magnetism in M layers, as well as the discovery of complex magnetism and giant magnetostriction in

Mn_2GaC [7]. However, to date, only a few compositions of magnetic MAX phases have been synthesized (mainly $(\text{Cr},\text{Mn})_2\text{AC}$ compositions), making it relevant both for theoretical search for stable magnetic MAX phases containing Mn, Fe, or Co, and for experimental realization of such compounds.

$\text{Cr}_{2-x}\text{Mn}_x\text{GeC}$ is one of the experimentally synthesized compositions known to exhibit long-range magnetic order in bulk and thin film form [13–17]. Magnetron sputtering is predominantly used for the fabrication of MAX phase films. There are numerous studies on the synthesis and investigation of epitaxial thin films of MAX phases [18], mainly with Ti [19–23] and Cr [12,24–28]. However, to the best of our knowledge, there is only one study on $\text{Cr}_{2-x}\text{Mn}_x\text{GeC}$ grown by magnetron sputtering on a heated MgO substrate under specific technological regime [17]. Nevertheless, the phase formation process depending on the synthesis conditions remains unexplored. Since substituted MAX phases are multi-component compounds, their synthesis—via sputtering—requires the complex adjustment of many parameters to achieve the desired stoichiometry and crystallographic orientation with respect to the substrate, which is crucial for the practical utilization of the unique properties of MAX phases for specific applications.

In this work, we present the results of systematic experimental investigations of the growth process and phase formation, as well as the influence of structure and morphology on the electronic, optical, and transport properties of Cr_2GeC and $\text{Cr}_{2-x}\text{Mn}_x\text{GeC}$ thin films prepared by magnetron sputtering.

2. Experimental Details

The samples were synthesized by magnetron co-sputtering from elemental targets of Cr (99.95%), Mn (99.95%), Ge (99.99%) and C (99.95%) (GIRMET Ltd., Moscow, Russia), positioned at a 60° angle to the substrate plane in an ultrahigh vacuum (UHV) chamber with a base pressure of 10^{-9} Torr. Deposition was performed in DC mode for the Cr, Mn, and C targets, and in RF mode for the Ge target. The high-purity argon (99.99995%) pressure was $7 \cdot 10^{-3}$ Torr. The average deposition rate, converted to bulk density, for all materials was approximately 2.5 nm/min. A single-crystal MgO (111) surface was used as a substrate. All samples underwent the same substrate preparation steps: (1) annealing in UHV at 700°C ; (2) Ar cleaning of the surface at room temperature with an Ar flow at a 60° angle to the substrate normal and continuous rotation around its axis; (3) brief annealing in UHV at 750°C immediately before deposition. The deposition was carried out at a substrate temperature of 650°C . After deposition, all samples were further annealed for 30 min in UHV at 850°C . The process was monitored in situ by reflection high-energy electron diffraction (RHEED) and Auger spectroscopy (AES).

The main synthesis conditions for each sample are listed in Table 1, where the film thickness D was calculated based on a bulk density of 6.5 g/cm^3 . The atomic stoichiometry of each element, obtained through preliminary calibration, corresponds to room temperature substrate conditions. After deposition, each sample was naturally cooled to room temperature under UHV conditions. Subsequently, it was removed from the vacuum chamber for characterization. X-ray diffraction (XRD) analysis was conducted using a PANalytical X'Pert PRO diffractometer equipped with a solid-state detector PIXcel on Cu $K\alpha$ radiation. Film morphology was studied using the atomic force microscopy (AFM) in tapping mode on a NanoInk DPN 5000 instrument. X-ray fluorescence (XRF) data was obtained using a local X-ray fluorescence spectrometer MC50M (Amtertek) and additional PXRF software (version 5.0.0). The concentrations of chromium, manganese, and germanium were calculated based on the fundamental parameters method of Sherman [29] with matrix effects corrected by the integral intensities of the main lines (100% normalization). The integral intensities were calculated by approximating the Gaussian peaks of the Cr $K\alpha_1$, Cr $K\alpha_2$, and Ge $K\alpha_1$ lines. Transport properties measurements were performed using the Van der Paul method [30]. EPO-TEK H20E silver epoxy was used to connect the external wiring to the $4 \times 4 \text{ mm}^2$ samples. A SourceMeter Keithley 2400 and a Nanovoltmeter Keithley 2182A were used as the current source and for voltage sensing. Hall voltage

measurements were conducted in the external magnetic field ranging from -9 to $+9$ T. The current-reversal method was used to subtract the thermoelectric component from the Hall voltage. The source current for the resistivity and Hall voltage measurements was 1 mA. During resistivity and Hall measurements at the variable temperature, the latter was changed from low to high by quasi-static warm up using PPMS cryostat. Optical properties were measured at room temperature in air by spectral ellipsometer Ellipse-1891 (ISP SB RAS). A 150 W Xe lamp (Hamamatsu) was used as a light source [31]. To improve the signal-to-noise ratio, the optical path of the ellipsometer was modified. The ellipsometric spectra were recorded in the range from 320 to 900 nm, with an angle of incidence of 44.7° and 61.7° relative to the sample's normal. The optical parameters, n and k , were calculated using an optical model of a homogeneous isotropic layer with a thickness of about D [32] on the isotropic MgO substrate surface [33].

Table 1. Synthesis parameters of the Cr_2GeC and $\text{Cr}_{2-x}\text{Mn}_x\text{GeC}$ thin films.

#	Atomic Stoichiometry, %				D, nm	Deposition Method	
	Cr	Mn	Ge	C			
1	49.7	-	25.6	24.6	10	continuous	
2	50	-	25.2	24.8			
3	50.1	-	19.7	30.2			
4	54.4	-	20.3	25.3			
5	54.4	-	20.3	25.3	40		
6	54.4	-	20.3	25.3	100		
7	55	-	16.8	28.2	40		
8	55	-	16.8	28.2	40.6		15 cycles of 2.7 nm with pauses of 1 min between sublayers
9	40.6	14.1	17	28.3	40.6		

3. Results and Discussion

3.1. Phase Composition and Morphology

The first step of characterization involved the atomic force microscopy (AFM) measurements after removing the samples from the chamber. The roughness analysis of the AFM data was performed using the Gwyddion software (version 2.61). As shown in Figure 1a–i, samples #1 ÷ #4 and #9 exhibited similar surface morphology, representing a typical granular film structure. To eliminate the influence of low frequencies arising from substrate roughness, the data were filtered using a low-pass filter. It can be said that the surface of samples #1 ÷ #4 and #9 had a similar morphology and consisted of rounded grains with sizes ranging from 20 nm to 70 nm. Individual grains were observed with heights h_g of 4.28 ± 0.64 nm (#1); 5.64 ± 0.30 nm (#2); 13.37 ± 1.97 nm (#3); 8.52 ± 1.46 nm (#4) and 25.32 ± 2.35 nm (#9). Samples #1 and #2 with close atomic ratios of Cr:Ge:C had very close morphology. The increasing of C (#3) or Cr (#4) content led to the increasing of grain height and size. Samples #5 ÷ #8 exhibited a different morphology. With an increasing thickness from 10 nm to 40 nm, the morphology changed. Sample #5 (Figure 1e) consisted of grains with an approximate diameter D_g of 25 nm and rods with lengths L_r ranging from 100 nm to 150 nm and diameters D_r ranging from 40 nm to 100 nm. The rods were oriented at an angle ϕ_r divisible by 30° to each other and at an angle of 3° to the substrate surface. Under the same technological stoichiometry for #5 and #6, increasing the thickness by a factor of 2.5 to 100 nm led to significant changes. Figure 1f shows that sample #6 contained plates with diameters D_p ranging from 100 nm to 300 nm, inclined at an angle of approximately 1.85° to the substrate surface. From these plates grew elongated crystal bars with a length of about ($L_b \approx 150$ nm, D_r from 40 nm to 100 nm), as well as rods

turned to each other at an angle (ϕ_b). It was evident that, with an increasing thickness, the plates and a portion of the rods combined to form larger crystallites. The deviation at an angle of 1.85° may be related to the crystallographic reorientation of the substrate. Sample #7 Figure 1g, having the same thickness as #5, but higher carbon content, consisted of elongated rounded grains predominantly oriented in the same direction. Sample #8 Figure 1h exhibited a similar morphology to #7. Significant change in crystallite size was observed when adding manganese to sample #9 (Figure 1i), indicating a change in the thermodynamics of film formation, substituted with the MAX phase compared to pure Cr_2GeC . The main details of the film morphology and the root mean square (Sq) value of the height irregularities, which provides information about the standard deviation of the grain size, are presented in Table 2.

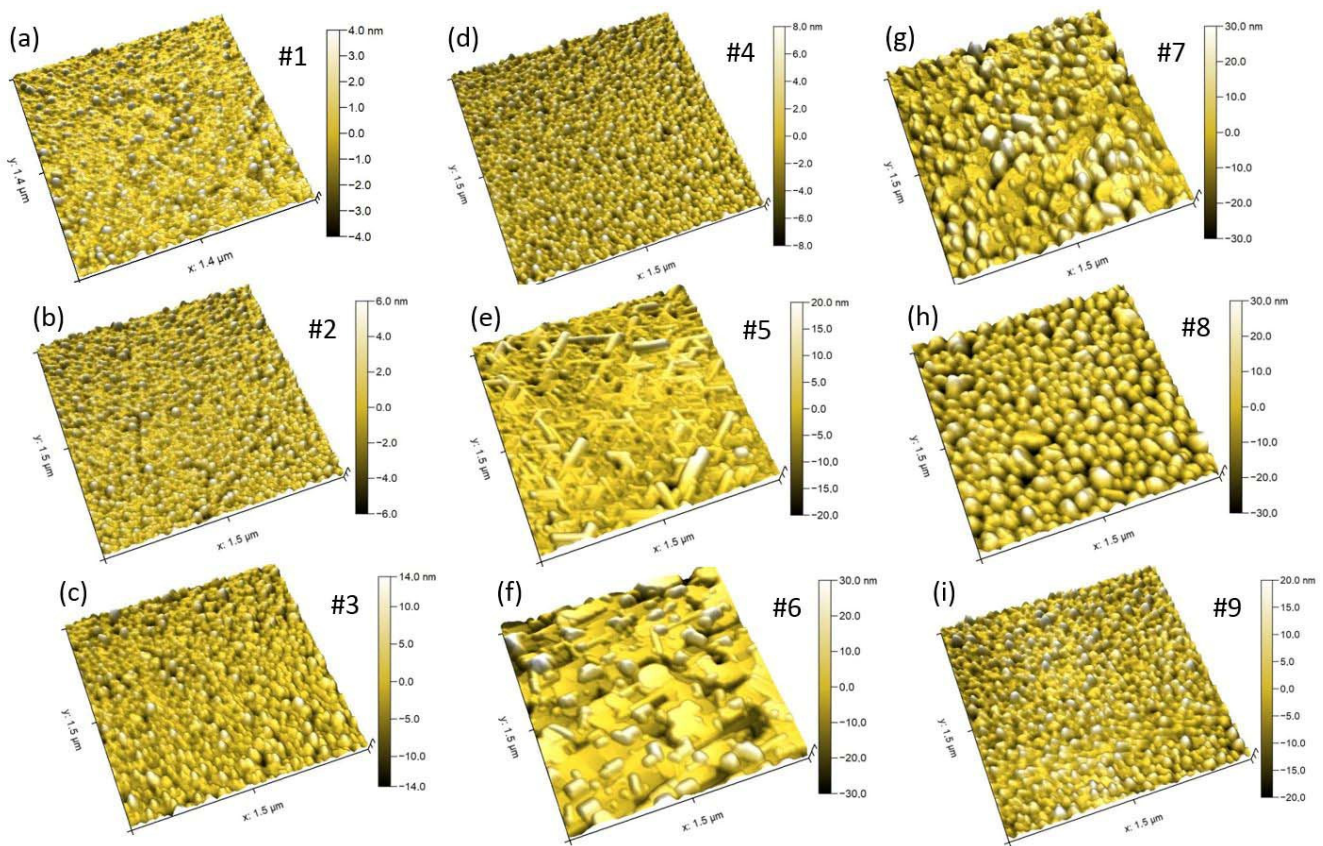


Figure 1. AFM image of the Cr_2GeC and $\text{Cr}_{2-x}\text{Mn}_x\text{GeC}$ thin films on $\text{MgO}(111)$. The images represent a frame size of $1.5 \times 1.5 \mu\text{m}^2$. The zero position on the pseudo-color ruler is chosen in the middle of the displayed height of the unevenness of thin films. Subfigures from (a–i) are corresponds to samples from #1 to #9.

After preliminary AFM characterization for samples #4–#9, X-ray diffraction (XRD) analysis was performed. It was found that all samples predominantly consisted of the Cr_2GeC MAX phase (ICDD 00-018-0384) and two chromium germanide phases, CrGe (ICDD 04-004-7750) and Cr_3Ge (ICDD 01-070-2924) (Figure 2). For samples #5 to #7 and #9, the Cr_2GeC phase was textured on the basal plane of the substrate, and reflections from the (013) texture were also observed, which formed on the lateral facets of MAX crystallites previously formed on the substrate. It was possible that a similar mechanism was responsible for the formation of CrGe crystallites, as indicated by the AFM data for samples #5 and #6. In addition to the flat islands with the diameters of $100 \div 300 \text{ nm}$, rods were observed, which were slightly inclined to the normal with lengths of $100 \div 150 \text{ nm}$ and diameters of $40 \div 60 \text{ nm}$, growing at an angle of approximately $0^\circ \pm 60^\circ$ to the $[210]_{\text{MgO}}$ direction. Notably, in sample #5, unlike #6, these thin rods protrude significantly

above the film surface (Figure 1e). It can be assumed that these rods in samples #5 and #6 corresponded to chromium germanides CrGe and Cr₃Ge.

Table 2. Synthesis parameters, morphology, phase composition, and chemical composition of the Cr₂GeC and Cr_{2-x}Mn_xGeC thin films.

#	Atomic Stoichiometry, %				D, nm	Deposition Method	RHEED	XRD	AFM	XRF Cr/Ge Atomic Ratio
	Cr	Mn	Ge	C						
1	49.7	-	25.6	24.6	10	continuous	-	-	Spherical grains $D_g = 20 \div 50$ nm, $h_g = 4.28 \pm 0.64$ nm; Sq = 1.024 nm	1.66 ± 0.40
2	50.0	-	25.2	24.8	Cr ₂ GeC [100] Cr ₂₃ C ₆ [210]		-	Spherical grains $D_g = 15 \div 45$ HM, $h_g = 5.64 \pm 0.30$ nm; Sq = 1.549 nm	1.92 ± 0.58	
3	50.1	-	19.7	30.2	Cr ₂ GeC [001] Cr ₂ GeC [100] + stripes		-	Spherical grains $D_g = 20 \div 50$ nm, $h_g = 13.37 \pm 1.97$ nm; Sq = 3.110 nm	2.01 ± 0.52	
4	54.4	-	20.3	25.3	Cr ₂ GeC [100] CrGe [100]		Cr ₃ Ge(002)	Spherical grains $D_g = 20 \div 70$ nm, $h_g = 8.52 \pm 1.46$ nm; Sq = 2.304 nm	7.47 ± 2.38	
5	54.4	-	20.3	25.3	40		Cr ₂ GeC [001] Cr ₂ GeC [100] + stripes	Cr ₂ GeC(00L) + CrGe(012) + weak Cr ₂ GeC(013)	Spherical grains $D_g = 15 \div 30$ nm; Rods $L_r = 100 \div 150$ HM, $D_r = 40 \div 100$ nm, $\phi_r = N \cdot 30^\circ$; $h_g = 1 \div 1.5$ nm; Sq = 4.031 nm	1.88 ± 0.31
6	54.4	-	20.3	25.3	100		Cr ₂ GeC	Cr ₂ GeC(00L) + CrGe(012) + Cr ₂ GeC(013)	Incline plates $D_p = 100 \div 300$ nm, $h_p = 30$ nm; bars $L_b = 100 \div 150$ nm $D_b = 40 \div 100$ nm, $\phi_b = N \cdot 30^\circ$; Sq = 8.553 nm	1.47 ± 0.37
7	55.0	-	16.8	28.2	40		Cr ₂ GeC [100]; CrGe [100]	Cr ₂ GeC(00L) + Cr ₂ GeC(013)	Elongated grains $D_g = 40 \div 90$ nm, $h_g = 2 \div 20$ nm; Sq = 8.490 nm	2.59 ± 0.48
8	55.0	-	16.8	28.2	40.6		Cr ₂ GeC [100]; CrGe [100]	Cr ₃ Ge(002) + CrGe(012) + Cr ₂ GeC(013)	Elongated grains $D_g = 40 \div 100$ nm, $h_g = 4 \div 12$ nm; Sq = 9.329 nm	2.17 ± 0.41
9	40.6	14.1	17.0	28.3	40.6		15 cycles of 2.7 nm with pauses of 1 min between sublayers	dots and stripes Cr ₂ GeC + dots CrGe	Cr ₂ GeC(00L) + Cr ₂ GeC(013)	Spherical grains $D_g = 30 \div 70$ nm, $h_g = 25.32 \pm 2.35$ nm; Sq = 2.864 nm

In addition to XRD analysis, reflection high-energy electron diffraction (RHEED) patterns were analyzed during the growth process. These patterns represented an ordered set of points, characteristic of a rough-textured film. Weak streaks were observed for samples #3, #5, and #9, indicating continuous regions in the epitaxial film. For most samples, the point reflections were well described by the Cr₂GeC MAX phase, while some samples exhibited reflections from chromium germanides or carbides. Furthermore, in situ measured Auger electron spectroscopy (AES) analysis confirmed the presence of all components in the thick films #5–#9, except for sample #8.

All data related to the structure, morphology, and chemical composition evaluated from X-ray fluorescence (XRF) data is presented in Table 2. Based on RHEED and XRD data, the presence of a pure MAX phase can be noted in samples #7 and #9, which have a high carbon content (over 28 at.%). In these cases, the carbon content was increased during synthesis to reduce the likelihood of germanide formation. Analyzing the XRF data,

it should be noted that, considering the error, both samples exhibited an atomic ratio of M/A close to the ideal stoichiometry. It can be concluded that deposition rates and heating conditions have little influence on phase formation. The atomic ratios of Cr:Ge:C were likely to play a significant role in the formation of the thin film MAX phase, and a slight excess of carbon was required for a successful MAX phase synthesis. Comparing samples #8 and #9, it was important to note that the addition of the fourth element significantly altered the course of the solid-state reaction. Sample #8 exhibited a more pronounced division of the film into multiple phases, while for sample #9, only peaks corresponding to the MAX phase were present in the X-ray diffraction pattern. In the specific case of $\text{Cr}_{2-x}\text{Mn}_x\text{GeC}$, the manganese-substituted composition was thermodynamically more stable than pure Cr_2GeC under the given synthesis conditions, resulting in the formation of the desired phase in sample #9. This assumption was consistent with theoretical calculations performed in [17], which demonstrated a decrease in the formation energy ΔG with the substitution of chromium by manganese at high synthesis temperatures.

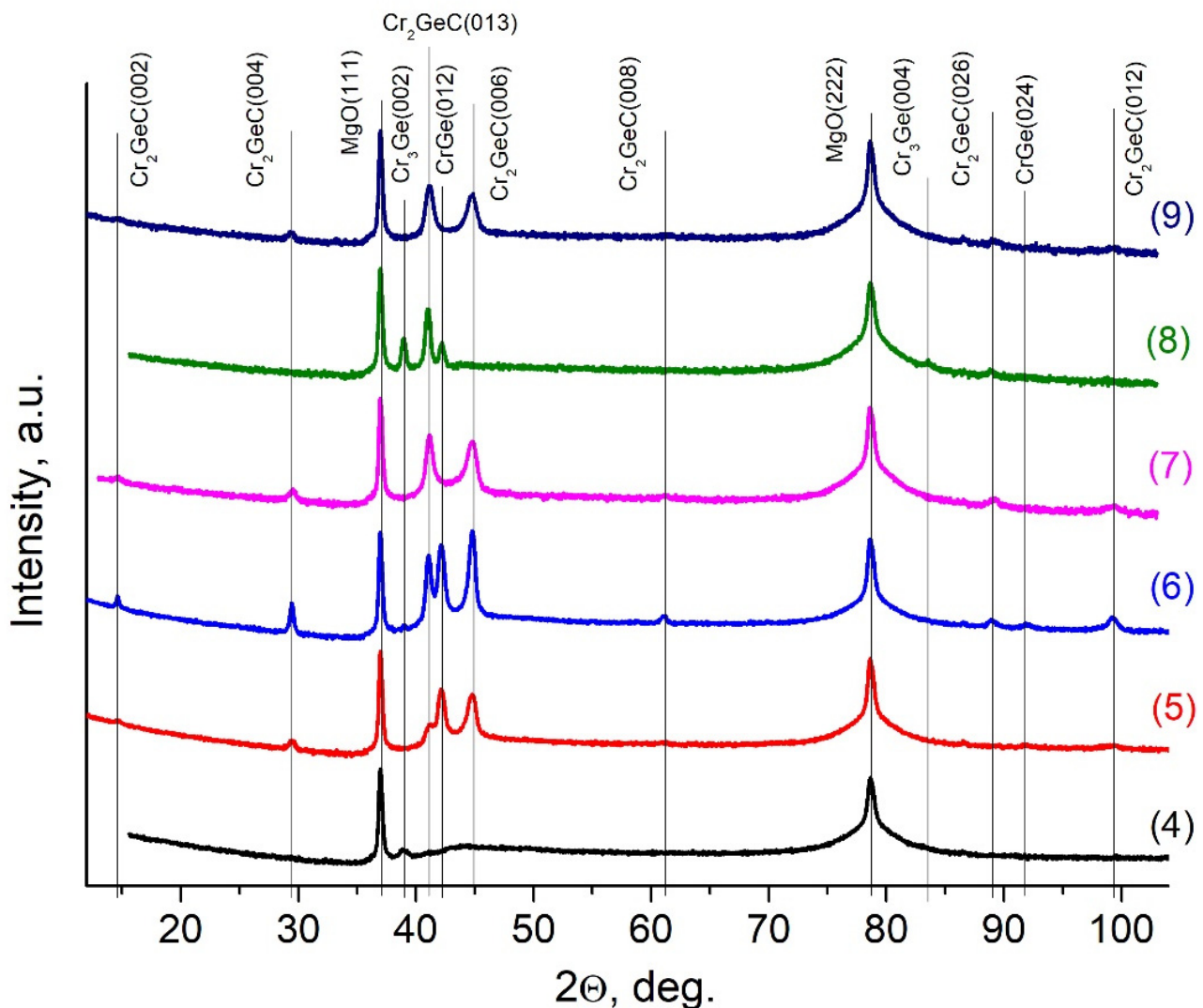


Figure 2. XRD profiles for samples #4–#9.

3.2. Optical and Transport Properties

The spectra of the refractive index n and absorption coefficient k of the synthesized films are presented in Figure 3. Among the optical properties, sample #5 stood out, exhibiting a plasmon peak in the range of $200 \div 300$ nm, which was likely a result of the effect of protruding CrGe rods observed in the AFM images on the optical properties of the film.

Similar faint peaks, possibly attributed to the film morphology, were visible in the spectra of all samples, except for #6 and #9. The characteristic long-wavelength slope of the Drude peak in the k spectra indicated metallic conductivity of the films in samples #1, #5 ÷ #7, and #9. Sample #9 was of particular interest due to its lowest optical absorption k but relatively high refractive index n , which may be due to the larger grain size with the low grain boundary defect density [34]. Materials with such a high refractive index were relevant for the development of visible light localization devices, such as light-emitting diodes [35], and structures with gradients n and k for solar energy applications [36]. Sample #6, with a thickness of 100 nm, showed the highest values of n and k , for which bulk optical properties and a weak contribution of surface morphology already predominated, which was due to the light entering the ellipsometer aperture, mainly reflected from flat epitaxial crystallites. The samples #2 ÷ #4, likely having low conductivity due to their small thickness and high film dispersion, exhibited the lowest k values.

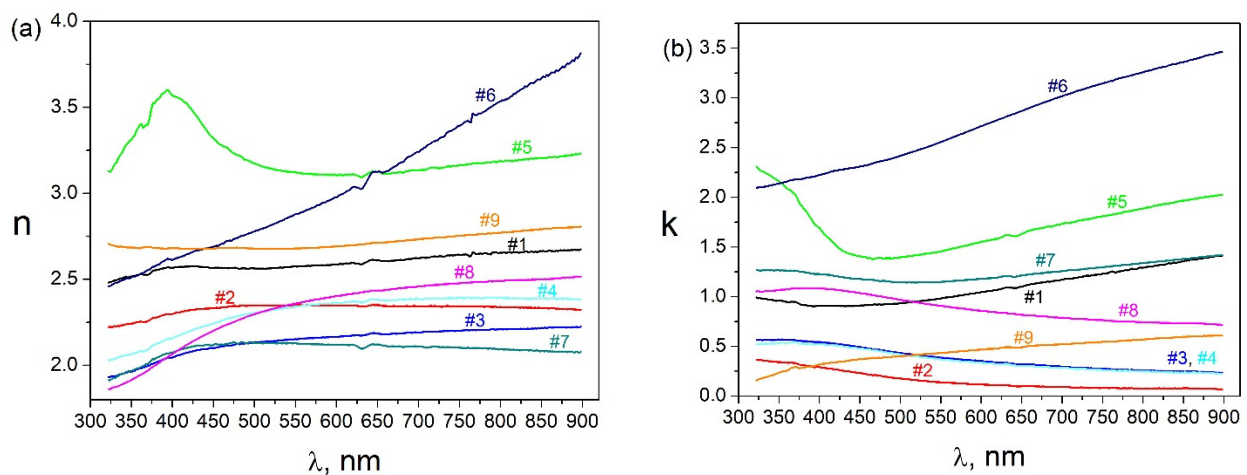


Figure 3. Refractive indices n (a) and absorption indices k (b) of Cr_2GeC and $(\text{Cr}_{0.75}\text{Mn}_{0.25})_2\text{GeC}$ films.

Transport and magnetotransport properties of the synthesized thin films of pure and manganese-substituted Cr_2GeC MAX phase were investigated. Samples #2 ÷ #4 demonstrated zero conductivity, which correlated with low k values and can be attributed to a low thickness and island-like film morphology. The resistivity ρ of samples #1 and #5 ÷ #7, regardless of their thickness, exhibited metallic behavior, decreasing with decreasing temperature (300 K ÷ 4 K) (Figure 4). Sample #1 had the lowest resistivity ρ , which can be interpreted as the presence of pure Cr in addition to the MAX phase in the film. The ρ value for films #5 ÷ #7 at 300 K varied in the range of 1.4 ÷ 1.8 $\mu\Omega\cdot\text{m}$, which was a typical value for MAX phases (0.5 ÷ 4 $\mu\Omega\cdot\text{m}$), close to the values for Mn_2GaC (2.9 $\mu\Omega\cdot\text{m}$) and CrMnGaC (1.6 $\mu\Omega\cdot\text{m}$)—which we investigated earlier—and consistent with literature data. For the epitaxial Cr_2GeC film of 180 nm thickness, P. Eklund et al. measured 0.6 $\mu\Omega\cdot\text{m}$ [25], while M. Barsoum et al. measured 0.7 $\mu\Omega\cdot\text{m}$ for the bulk phase [37]. The observed increase in ρ with a decreasing thickness in our case was directly related to the crystalline quality of the films and their microstructure, which was consistent with the optical measurements. Additionally, as the thickness decreased, the residual resistance ratio (RRR) factor (the ratio of resistance at 300 K to 4 K) decreased, indicating a greater contribution of scattering on defects and boundaries for thinner films. Considering the structural data and transport properties, it can be concluded that samples #5 ÷ #7 exhibited a high crystalline quality despite the presence of the CrGe phase in samples #5 and #6, according to XRD. Our conclusion was based on the fact that CrGe had two times higher resistivity and a very high RRR value of 260 [38]. However, no significant increase in ρ and RRR was observed for our films. Therefore, the CrGe phase did not make a significant contribution to the transport properties in samples #5 and #6.

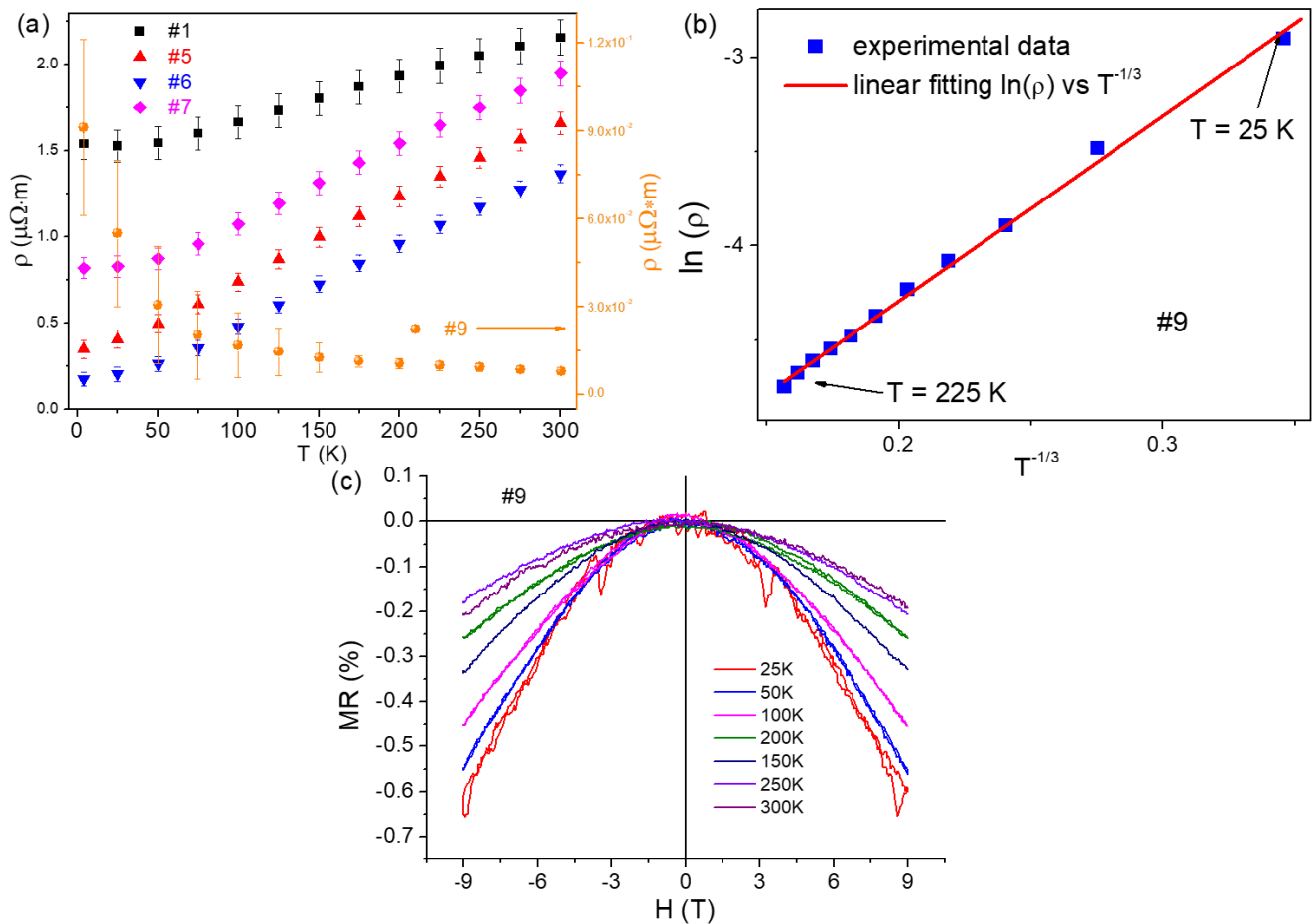


Figure 4. (a) Resistivity of Cr_2GeC and $(\text{Cr,Mn})_2\text{GeC}$. (b) $\ln(\rho)$ vs $T^{-1/3}$ dependence illustrating 2D hopping conduction mechanism for sample #9. (c) Magnetoresistance dependences for sample #9.

The resistivity behavior of the manganese-substituted sample $(\text{Cr,Mn})_2\text{GeC}$ #9 was fundamentally different, increasing with a decreasing temperature and being four orders of magnitude higher than ρ for Cr_2GeC (Figure 4a). Semiconductor-like behavior was previously observed for 20 nm thick Cr_2AlC films, while a transition to metallic conductivity occurred for a film thickness of 36 nm [27]. Such behavior was caused by the coalescence of crystallites. In our case, $(\text{Cr,Mn})_2\text{GeC}$ had a different morphology compared to Cr_2AlC , and, as a result, poor coalescence occurred in sample #9 with a thickness of 40 nm. The relatively low k and high n values in its optical spectra, along with the AFM data, indirectly indicated the presence of large crystallites. The temperature dependence of ρ for sample #9 was well described by the $\ln(\rho)$ vs $T^{-1/3}$ curve (Figure 4b), suggesting a 2D Mott hopping conduction mechanism [39]. Therefore, it can be assumed that in the regions where large crystallites connected, the film thickness h_{hop} was significantly smaller than the overall thickness of $(\text{Cr,Mn})_2\text{GeC}$. Additionally, these areas likely had a high number of defects. Based on the AFM data, the sizes and heights of the grains were known, which allowed estimating the h_{hop} approximately as 10–15 nm. The additional experimental fact proofing hopping conduction mechanism was negative magnetoresistance (MR) observed in the whole temperature region (Figure 4c). Moreover, the independence of the shape of the MR curves from temperature eliminated the dominant contribution of quantum corrections to conductivity like localization or antilocalization, which appeared at low temperatures [40]. Negative MR usually appeared in ferromagnetic materials or materials with complex magnetic structures [41], like non-compensated or non-collinear antiferromagnets. The latter can be realized in magnetic MAX phases [7] and, in particular, in $(\text{Cr,Mn})_2\text{GeC}$.

The Hall effect (Figure 5a) and magnetoresistance were measured for the conducting samples over a wide temperature range (4 K ÷ 300 K) and magnetic field up to 9 T. The Hall constant R_H , mobility μ , and charge carrier concentration n were calculated (Figure 5b), using the standard expressions:

$$\frac{V_H}{I}(H) = R_H \frac{H}{d} \quad (1)$$

$$R_H = \frac{1}{Ne} = \mu\rho \quad (2)$$

where I and V_H were the bias current and voltage measured in standard Van der Paul geometry, H and d were the magnetic field and film thickness, e was the elementary charge, and N was the carriers' concentration.

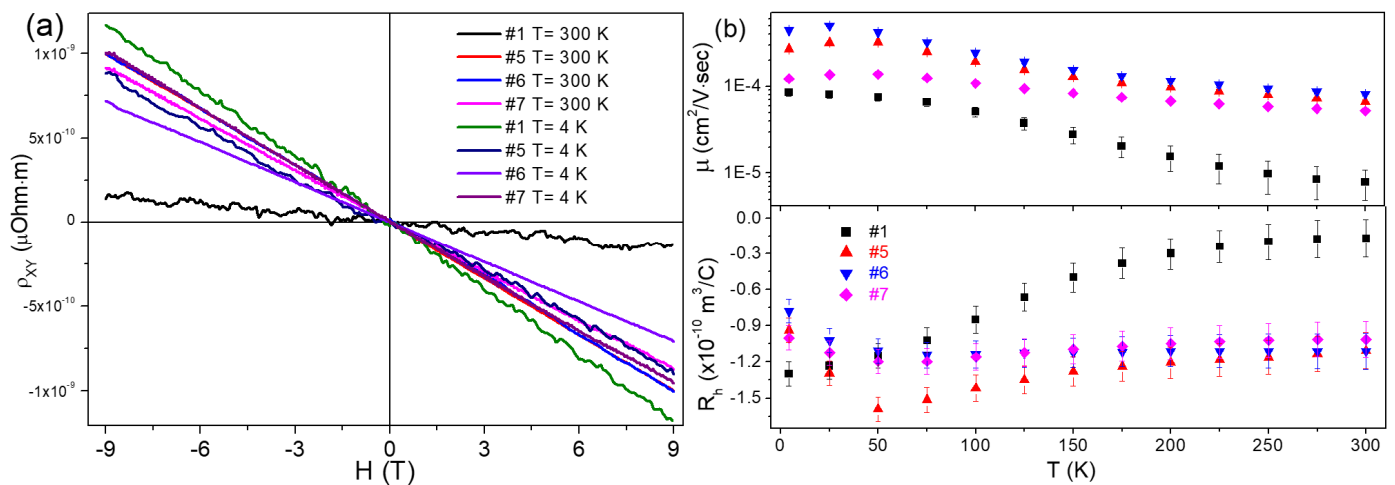


Figure 5. (a) Hall resistivity. (b) Mobility μ (top panel) and Hall coefficient R_H (bottom panel) for Cr_2GeC films.

The mobility for all Cr_2GeC samples was in the range of a few $\text{cm}^2/\text{V}\cdot\text{s}$ which was a typical value for metals. It should be noted that the temperature dependence of mobility exhibited a non-monotonic behavior, showing a maximum around 40 ÷ 50 K. Similar behavior was observed for bulk samples and was likely associated with an electron–electron scattering component [14]. The calculated carrier concentration N was very high; for example, for sample #6, the concentration at 4.2 K was close to the electron concentration for copper, which was $\sim 8.4 \times 10^{28} \text{ 1/m}^3$.

MAX phases are known to have a complex Fermi surface [42,43], resulting in the presence of both electrons and holes from the occupied electron band and four hole bands at the Fermi level. Therefore, to accurately calculate the transport parameters, a two-zone model [42] that considered both electron and hole contributions to conductivity was necessary:

$$R_H = \frac{P\mu_p^2 - N\mu_n^2}{e(P\mu_p^2 + N\mu_n^2)} \quad (3)$$

where P was the hole concentration, N was the electron density, μ_p and μ_n were the hole and electron mobility correspondingly. Taking into account different types of carriers with different dispersion of the wave vector, the nonmonotonic temperature dependence of μ was most likely due to the different low-temperature behavior of electrons and holes, resulting in the competing contributions to the Hall voltage.

Using the assumption that the mobility of electrons and holes was equal to the square root of the magnetoresistance (MR) coefficient $\mu_n = \mu_p = \sqrt{\alpha}$ ($\text{MR} \sim \alpha \cdot H^2$) [37], the values of μ , N , and P were recalculated for the samples with the best phase composition and conductivity (Figure 6). In this approximation, we obtained more reasonable values N and

P for a low-conductivity metal in the range of $10^{26} \div 10^{27} \text{ 1/m}^3$, which were close to the values calculated in the same way for the bulk polycrystal Cr_2GeC [37] and single crystal Cr_2AlC [42]. Meanwhile, the calculated mobility μ was one order of magnitude higher than those for bulk polycrystalline samples and was about $125 \text{ cm}^2/\text{V}\cdot\text{s}$ for the Cr_2AlC single crystal at room temperature [42]. This suggested that the high crystal quality of the film positively affected the mobility of charge carriers. It is important to note that the low-temperature data (below 50 K) presented in Figure 6a,b may be distorted by the calculation method used, which assumed that the magnetoresistance in the sample was caused solely by the Lorentz force. However, at low temperatures, even in non-ferromagnetic materials, there are contributions to the magnetoresistance associated with quantum corrections to conductivity, which can be both positive and negative [40], strongly affecting the accuracy of determining α and, consequently, μ , N , and P .

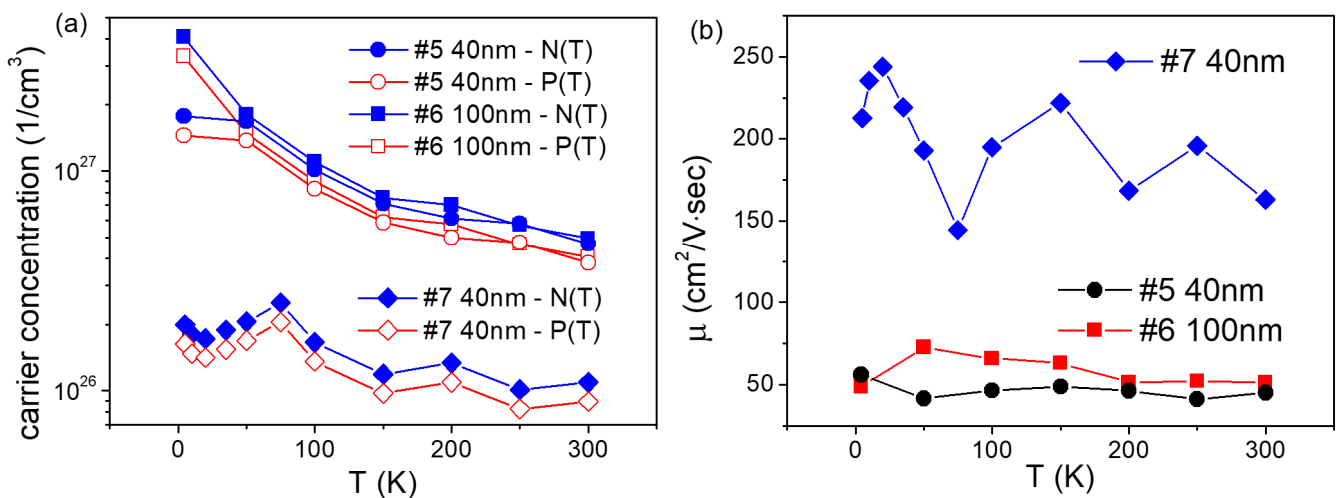


Figure 6. Temperature dependences of the charge carrier concentrations N and P (a) and mobility μ (b) for the Cr_2GeC films.

4. Conclusions

Cr_2GeC and $\text{Cr}_{2-x}\text{Mn}_x\text{GeC}$ thin films were synthesized using the magnetron sputtering technique. The growth characteristics, phase formation, and the influence of structure and morphology on the electronic, optical, and transport properties were investigated. It was observed that the deposition rates and heating regimes had a weak effect on phase formation as long as the temperature exceeded $650 \text{ }^\circ\text{C}$, allowing for the reaction to occur. Most likely, the Cr:Ge:C atomic ratios played the main role in the formation of a thin film of the MAX phase. A slight excess of carbon favored the formation of the Cr_2GeC MAX phase. Increasing the film thickness resulted in significant changes in morphology, leading to the development of faceted crystallites. Furthermore, doping the films with manganese was found to induce additional changes in morphology and improve the phase composition, as revealed by AFM and XRD data. Based on optical spectra, resistivity, and Hall measurements, it was determined that Cr_2GeC films with a thicknesses exceeding 40 nm exhibited metallic behavior. The $\text{Cr}_{2-x}\text{Mn}_x\text{GeC}$ film demonstrated a hopping-type conduction mechanism, which may be attributed to the columnar form of crystallites. Using a two-band model, the concentration of electrons and holes in the well-synthesized Cr_2GeC films was estimated to be $\sim 10^{27} \text{ cm}^{-3}$. The carrier mobility μ of approximately $200 \text{ cm}^2/\text{V}\cdot\text{sec}$ was one order of magnitude higher than that of bulk polycrystal, indicating the high crystal quality of the thin films. Overall, this systematic study of $\text{Cr}_{2-x}\text{Mn}_x\text{GeC}$ thin films contributed to a better understanding of the growth processes of MAX phases and holds promise for the development of robust conductive and protective coatings.

Author Contributions: Conceptualization, A.S.T., S.A.L. and S.N.V.; data curation, A.S.T., S.A.L., M.V.R., A.V.L. and T.A.A.; formal analysis, M.V.R., A.V.L., T.A.A., O.A.M. and M.A.B.; funding acquisition, S.G.O. and S.N.V.; investigation, A.S.T., S.A.L., M.V.R., A.V.L., T.A.A., L.A.S., I.A.Y., D.V.S., M.A.B. and I.A.B.; methodology, A.S.T., S.A.L. and M.V.R.; project administration, S.N.V.; resources, A.S.T. and S.G.O.; software, S.A.L. and M.V.R.; supervision, S.N.V.; writing—original draft, A.S.T., S.A.L. and A.V.L.; Writing—review & editing, A.S.T., S.A.L. and S.N.V. All authors have read and agreed to the published version of the manuscript.

Funding: This study was supported by the Russian Science Foundation, project no. 21-12-00226.

Data Availability Statement: The data that support the findings of this study are available upon reasonable request from the authors.

Acknowledgments: The authors thank the laboratory of the Magnetic MAX Materials created under the Megagrant project (agreement no. 075-15-2019-1886) for providing experimental equipment and the Collective Use Center at the Krasnoyarsk Scientific Center (Siberian Division, Russian Academy of Sciences) for assistance.

Conflicts of Interest: The authors declare no conflict of interest.

References

1. Geim, A.; Novoselov, K. The rise of graphene. *Nat. Mater.* **2007**, *6*, 183–191. [[CrossRef](#)]
2. Zhang, K.; Feng, Y.; Wang, F.; Yang, Z.; Wang, J. Two dimensional hexagonal boron nitride (2D-hBN): Synthesis, properties and applications. *J. Mater. Chem. C* **2017**, *5*, 11992–12022. [[CrossRef](#)]
3. Shi, Y.; Li, H.; Li, L.J. Recent advances in controlled synthesis of two-dimensional transition metal dichalcogenides via vapour deposition techniques. *Chem. Soc. Rev.* **2015**, *44*, 2744–2756. [[CrossRef](#)] [[PubMed](#)]
4. Naguib, M.; Barsoum, M.W.; Gogotsi, Y. Ten Years of Progress in the Synthesis and Development of MXenes. *Adv. Mater.* **2021**, *33*, 2103393. [[CrossRef](#)]
5. VahidMohammadi, A.; Rosen, J.; Gogotsi, Y. The world of two-dimensional carbides and nitrides (MXenes). *Science* **2021**, *372*, eabf1581. [[CrossRef](#)] [[PubMed](#)]
6. Sokol, M.; Natu, V.; Kota, S.; Barsoum, M.W. On the chemical diversity of the MAX phases. *Trends Chem.* **2019**, *1*, 210–223. [[CrossRef](#)]
7. Novoselova, I.P.; Petruhins, A.; Wiedwald, U.; Ingason Á, S.; Hase, T.; Magnus, F.; Kapaklis, V.; Palisaitis, J.; Spasova, M.; Farle, M.; et al. Large uniaxial magnetostriction with sign inversion at the first order phase transition in the nanolaminated Mn₂GaC MAX phase. *Sci. Rep.* **2018**, *8*, 2637. [[CrossRef](#)]
8. Flatten, T.; Matthes, F.; Petruhins, A.; Salikhov, R.; Wiedwald, U.; Farle, M.; Rosen JBürgler, D.E.; Schneider, C.M. Direct measurement of anisotropic conductivity in a nanolaminated (Mn_{0.5}Cr_{0.5})₂GaC thin film. *Appl. Phys. Lett.* **2019**, *115*, 094101. [[CrossRef](#)]
9. Jubert, P.O.; Santos, T.; Le, T.; Ozdol, B.; Papisoi, C. Anisotropic Heatsinks for Heat-Assisted Magnetic Recording. *IEEE Trans. Magn.* **2020**, *57*, 1–5. [[CrossRef](#)]
10. Barsoum, M.W.; Radovic, M. Elastic and mechanical properties of the MAX phases. *Annu. Rev. Mater. Res.* **2011**, *41*, 195–227. [[CrossRef](#)]
11. Tunes, M.A.; Imtyazuddin, M.; Kainz, C.; Pogatscher, S.; Vishnyakov, V.M. Deviating from the pure MAX phase concept: Radiation-tolerant nanostructured dual-phase Cr₂AlC. *Sci. Adv.* **2021**, *7*, eabf6771. [[CrossRef](#)]
12. Imtyazuddin, M.; Mir, A.H.; Tunes, M.A.; Vishnyakov, V.M. Radiation Resistance and Mechanical Properties of Magnetron-Sputtered Cr₂AlC Thin Films. *J. Nucl. Mater.* **2019**, *526*, 151742. [[CrossRef](#)]
13. Liu, Z.; Waki, T.; Tabata, Y.; Nakamura, H. Mn-doping-induced itinerant-electron ferromagnetism in Cr₂GeC. *Phys. Rev. B* **2014**, *89*, 054435. [[CrossRef](#)]
14. Lin, S.; Huang, Y.; Zu, L.; Kan, X.; Lin, J.; Song, W.; Tong, P.; Zhu, X.; Sun, Y. Alloying effects on structural, magnetic, and electrical/thermal transport properties in MAX-phase Cr₂-xM_xGeC (M = Ti, V, Mn, Fe, and Mo). *J. Alloys Compd.* **2016**, *680*, 452–461. [[CrossRef](#)]
15. Tao, Q.Z.; Hu, C.F.; Lin, S.; Zhang, H.B.; Li, F.Z.; Qu, D.; Wu, M.L.; Sun, Y.; Sakka, Y. Coexistence of Ferromagnetic and a Re-entrant Cluster Glass State in the Layered Quaternary (Cr_{1-x}Mn_x)₂GeC. *Mater. Res. Lett.* **2014**, *2*, 192–198. [[CrossRef](#)]
16. Rivin, O.; Caspi, E.N.; Pesach, A.; Shaked, H.; Hoser, A.; Georgii, R.; Tao, Q.; Rosén, J.; Barsoum, M.W. Evidence for ferromagnetic ordering in the MAX phase (Cr_{0.96}Mn_{0.04})₂GeC. *Mater. Res. Lett.* **2017**, *5*, 465–471. [[CrossRef](#)]
17. Ingason, A.S.; Mockute, A.; Dahlqvist, M.; Magnus, F.; Olafsson, S.; Arnalds, U.B.; Alling, B.; Abrikosov, I.A.; Hjörvarsson, B.; Persson, P.O.; et al. Magnetic self-organized atomic laminate from first principles and thin film synthesis. *Phys. Rev. Lett.* **2013**, *110*, 195502. [[CrossRef](#)] [[PubMed](#)]
18. Biswas, A.; Natu, V.; Puthirath, A.B. Thin-film growth of MAX phases as functional materials. *Oxf. Open Mater. Sci.* **2021**, *1*, itab020. [[CrossRef](#)]

19. Wilhelmsson, O.; Palmquist, J.P.; Lewina, E.; Emmerlich, J.; Eklund, P.; Persson, P.; Högberg, H.; Li, S.; Ahuja, R.; Eriksson, O.; et al. Deposition and characterization of ternary thin films within the Ti–Al–C system by DC magnetron sputtering. *J. Cryst. Growth* **2006**, *291*, 290–300. [[CrossRef](#)]
20. Rosen, J.; Ryves, L.; Persson, P.O.A.; Bilek, M.M.M. Deposition of epitaxial Ti₂AlC thin films by pulsed cathodic arc. *J. Appl. Phys.* **2007**, *101*, 056101. [[CrossRef](#)]
21. Frodelius, J.; Eklund, P.; Beckers, M.; Persson, P.; Högberg, H.; Hultman, L. Sputter deposition from a Ti₂AlC target: Process characterization and conditions for growth of Ti₂AlC. *Thin Solid Films* **2010**, *518*, 1621–1626. [[CrossRef](#)]
22. Högberg, H.; Hultman, L.; Emmerlich, J.; Joelsson, T.; Eklund, P.; Molina-Aldareguia, J.M.; Palmquist, J.P.; Wilhelmsson, O.; Jansson, U. Growth and characterization of MAX-phase thin films. *Surf. Coat Technol.* **2005**, *193*, 6–10. [[CrossRef](#)]
23. Azina, C.; Eklund, P. Effects of temperature and target power on the sputter-deposition of (Ti,Zr)_{n+1}AlC_n MAX-phase thin films. *Results Mater* **2021**, *9*, 100159. [[CrossRef](#)]
24. Petruhins, A.; Ingason, A.S.; Lu, J.; Magnus, F.; Olafsson, S.; Rosen, J. Synthesis and characterization of magnetic (Cr_{0.5}Mn_{0.5})₂GaC thin films. *J. Mater. Sci.* **2015**, *50*, 4495–4502. [[CrossRef](#)]
25. Eklund, P.; Bugnet, M.; Mauchamp, V.; Dubois, S.; Tromas, C.; Jensen, J.; Piraux, L.; Gence, L.; Jaouen, M.; Cabioch, T. Epitaxial growth and electrical transport properties of Cr₂GeC thin films. *Phys. Rev. B* **2011**, *84*, 075424. [[CrossRef](#)]
26. Mockuté, A.; Dahlqvist, M.; Emmerlich, J.; Hultman, L.; Schneider, J.M.; Persson, P.O.; Rosén, J. Synthesis and ab initio calculations of nanolaminated (Cr, Mn)₂AlC compounds. *Phys. Rev. B* **2013**, *87*, 094113. [[CrossRef](#)]
27. Stevens, M.; Pazniak, H.; Jemiola, A.; Felek, M.; Farle, M.; Wiedwald, U. Pulsed laser deposition of epitaxial Cr₂AlC MAX phase thin films on MgO(111) and Al₂O₃(0001). *Mater. Res. Lett.* **2021**, *9*, 343–349. [[CrossRef](#)]
28. Pazniak, H.; Stevens, M.; Dahlqvist, M.; Zingsem, B.; Kibkalo, L.; Felek, M.; Varnakov, S.; Farle, M.; Rosen, J.; Wiedwald, U. Phase Stability of Nanolaminated Epitaxial (Cr_{1-x}Fe_x)₂AlC MAX Phase Thin Films on MgO (111) and Al₂O₃ (0001) for Use as Conductive Coatings. *ACS Appl. Nano Mater.* **2021**, *4*, 13761–13770. [[CrossRef](#)]
29. Rousseau, R.V. The fundamental algorithm: A natural extension of the Sherman equation Part 1: Theory/R.M. Rousseau, J.A. Boivin. *Rigaku J.* **1998**, *15*, 13–27.
30. Der Pauw, L.V. A Method of Measuring Specific Resistivity and Hall Effect of Discs of Arbitrary Shape. *Philips Res. Rep* **1991**, *13*, 1–9. [[CrossRef](#)]
31. Shevtsov, D.V.; Lyaschenko, S.A.; Varnakov, S.N. An ultrahigh-vacuum multifunctional apparatus for synthesis and in situ investigation of lowdimensional structures by spectral magnetoellipsometry in the temperature range of 85–900 K. *Instrum. Ex Tech.* **2017**, *60*, 759–763. [[CrossRef](#)]
32. Urban, F.K., III; Barton, D.; Tiwald, T. Numerical ellipsometry: Analysis of thin metal layers using n–k plane methods with multiple incidence angles. *Thin Solid Film.* **2009**, *518*, 1411. [[CrossRef](#)]
33. Stephens, R.E.; Malitson, I.H. Index of Refraction of Magnesium Oxide. *Res. Nat. Bur. Stand.* **1952**, *49*, 249. [[CrossRef](#)]
34. An, N.; Wang, K.; Wei, H.; Song, Q.; Xiao, S. Fabricating high refractive index titanium dioxide film using electron beam evaporation for all-dielectric metasurfaces. *MRS Commun.* **2016**, *6*, 77–83. [[CrossRef](#)]
35. Liu, J.-G.; Ueda, M. High refractive index polymers: Fundamental research and practical applications. *J. Mater. Chem.* **2009**, *19*, 8907–8919. [[CrossRef](#)]
36. Poobalan, R.K.; Barshilia, H.C.; Basu, B. Recent trends and challenges in developing boride and carbide-based solar absorbers for concentrated solar power. *Sol. Energy Mater. Sol. Cells* **2022**, *245*, 111876. [[CrossRef](#)]
37. Barsoum, M.W.; Scabarozzi, T.H.; Amini, S.; Hettinger, J.D.; Lofland, S.E. Electrical and thermal properties of Cr₂GeC. *J. Am. Ceram. Soc.* **2011**, *94*, 4123–4126. [[CrossRef](#)]
38. Klotz, J.; Götze, K.; Förster, T.; Bruin, J.A.N.; Wosnitzer, J.; Weber, K.; Schmidt, M.; Schnelle, W.; Geibel, C.; Rößler, U.K.; et al. Electronic band structure and proximity to magnetic ordering in the chiral cubic compound CrGe. *Phys. Rev. B* **2019**, *99*, 085130. [[CrossRef](#)]
39. Mott, N.F. Conduction in glasses containing transition metal ions. *Non-Cryst. Solids* **1968**, *1*, 1–17. [[CrossRef](#)]
40. Lee, A.; Ramakrishnan, T.V. Disordered electronic systems. *Rev. Mod. Phys.* **1985**, *57*, 287–337. [[CrossRef](#)]
41. Li, P.; Zhang, L.T.; Mi, W.B.; Jiang, E.Y.; Bai, H.L. Origin of the butterfly-shaped magnetoresistance in reactive sputtered epitaxial Fe₃O₄ films. *J. Appl. Phys.* **2009**, *106*, 033908. [[CrossRef](#)]
42. Ouisse, T.; Shi, L.; Piot, B.A.; Hackens, B.; Mauchamp, V.; Chaussende, D. Magnetotransport properties of nearly-free electrons in two-dimensional hexagonal metals and application to the M_{n+1}AX_n phases. *Phys. Rev. B* **2015**, *92*, 045133. [[CrossRef](#)]
43. Ouisse, T.; Barsoum, M.W. Magnetotransport in the MAX phases and their 2D derivatives: MXenes. *Mater. Res. Lett.* **2017**, *5*, 365–378. [[CrossRef](#)]

Disclaimer/Publisher’s Note: The statements, opinions and data contained in all publications are solely those of the individual author(s) and contributor(s) and not of MDPI and/or the editor(s). MDPI and/or the editor(s) disclaim responsibility for any injury to people or property resulting from any ideas, methods, instructions or products referred to in the content.